

Unifying supervised learning and VAEs - automating statistical inference in high-energy physics

Thorsten Glüsenkamp*

*Erlangen Centre for Astroparticle Physics (ECAP),
Friedrich-Alexander Universität Erlangen-Nürnberg,
Erlangen, Germany*

December 22, 2024

Abstract

A KL-divergence objective of the joint distribution of data and labels allows to unify supervised learning, variational autoencoders (VAEs) and semi-supervised learning under one umbrella of variational inference. This viewpoint has several advantages. For VAEs, it clarifies the interpretation of encoder and decoder parts. For supervised learning, it re-iterates that the training procedure approximates the true posterior over labels and can always be viewed as approximate likelihood-free inference. This is typically not discussed, even though the derivation is well-known in the literature. In the context of semi-supervised learning it motivates an extended supervised scheme which allows to calculate a goodness-of-fit p-value using posterior predictive simulations. Flow-based networks with a standard normal base distribution are crucial. We discuss how they allow to rigorously define coverage for arbitrary joint posteriors on $\mathbb{R}^n \times \mathcal{S}^m$, which encompasses posteriors over directions. Finally, systematic uncertainties are naturally included in the variational viewpoint. With the three ingredients of (1) systematics, (2) coverage and (3) goodness-of-fit, flow-based neural networks have the potential to replace a large part of the statistical toolbox of the contemporary high-energy physicist.

Contents

1	Introduction	2
2	Monte Carlo estimates and the joint KL-divergence	3
2.1	Supervised learning	3
2.2	Unsupervised learning: Variational autoencoders	4
2.3	Extended supervised or semi-supervised learning	6
3	Toy Monte Carlo	7
4	The importance of flow-based models	9
5	Systematic Uncertainties	10
6	Coverage of the neural network posterior	10
7	Goodness-of-Fit of the neural network model	13
8	Related Work	16
9	Conclusion	16
A	Implementation details	17
A.1	Training	17
A.2	Posterior	18
A.3	Likelihood	18
A.4	Parameter choices	18

*thorsten.gluesenkamp@fau.de

1 Introduction

Deep neural networks have achieved great results over the last couple of years. While the breakthroughs were initially made in industrial applications, for example in image processing [1], in recent years their application in fundamental science has become more and more ubiquitous. A typical application of deep learning in experimental high-energy physics is concerned with the reconstruction of particle interactions [2], for example inferring particle type, i.e. classification [3], or inferring direction, position and energy, i.e. regression [4]. Traditionally, reconstructions of continuous quantities are performed by parametrized likelihood fits [5] which allow to calculate confidence intervals with standard Frequentist or Bayesian methods [6]. Neural networks on the contrary are often used to produce point estimates [7], and there is no universal agreed-upon notion how to calculate confidence intervals. Often they are just ignored, the result is registered as an observable and used in a binned likelihood analysis [4]. Per-event uncertainties are not necessarily required for this use-case. However, there are many situations where precise uncertainty quantification is important. An example are per-event reconstructions in high-energy neutrino telescopes like IceCube [8] or gravitational-wave observatories like LIGO [9] in the context of multimessenger astronomy [10]. These experiments send out alerts to the astronomical community to perform follow-up observations with other experiments. On the one hand, these alerts are time-critical and should be sent out to the public as fast as possible. On the other hand, the uncertainties of the inferred direction must be precise and in particular not biased. While neural networks are very fast, the second condition is hard to fulfill with standard neural network architectures, since neural networks normally only make point predictions. A naive solution could employ Bayesian neural networks or approximations like certain dropout-variations [11] or ensemble-methods [12]. However, these methods model a posterior over network weights, not over the actual physics parameters. An alternative is to parametrize the likelihood function with a neural network and perform a standard likelihood-based Frequentist or Bayesian analysis. Recently, this was done for gravitational-wave signals with flow-based networks [13]. However, such methods inherit the disadvantages of likelihood-based inference, for example getting stuck in local optima during optimization or long running times of MCMC. An alternative that recently has gotten popular is likelihood-free inference with neural networks, in which the posterior is directly learned from data. This has been applied to gravitational wave posteriors modeling the posterior as a parametrized Gaussian or mixture of Gaussians [14] and going beyond to use autoregressive normalizing flows for more complex shapes [15]. This paper is about the same line of thinking, where the posterior or more generally parts of the joint distribution of data and labels are learnt using normalizing flows.

We first review that the training process in supervised learning can be recast as variational inference of the true posterior distribution over labels, where the variational approximation is parametrized by a neural network. The derivation involves the KL-divergence of the joint distribution of data and labels. This is a known derivation and the final loss function is sometimes called "conditional maximum-likelihood objective" in the machine learning literature [16]. While the loss indeed represents a likelihood with respect to the neural network parameters, we emphasize it is more useful to think of it as an approximation of the posterior over the latent variables. Standard supervised learning usually uses the mean-squared-error (MSE) loss function, which corresponds to a standard-normal posterior as an approximation of the true posterior. This is obviously a very bad approximation in most cases. We compare it to the slightly more complex case of a Gaussian with a single covariance parameter and in particular approximations based on normalizing-flows [17], which in principle have arbitrary approximation capabilities. Since all Gaussian approximations, including the basic MSE loss, can be thought of as special cases of normalizing flows, so-called *affine flows*, it seems sensible to view all supervised loss functions from this angle. While normalizing-flow base distributions can be arbitrary, it turns out that there are advantages of starting with a standard normal as a base distribution that go beyond the argument of simple evaluation. The standard normal automatically allows for straight-forward coverage tests, which is discussed in section 6.

Usually, variational inference with neural networks is employed in unsupervised learning in the context of variational autoencoders (VAEs). As we will show (section 2.2), one can derive the ELBO loss of a variational autoencoder from the same joint KL-divergence as the supervised "maximum likelihood objective". This new derivation sheds some light on the interpretation of VAEs. Additionally, semi-supervised learning can be derived from the same starting point (section 2.3). The loss function of semi-supervised learning is also related to something we call "extended supervised" learning, which allows to calculate Bayesian goodness-of-fit values (section 7).

The unified viewpoint merges traditional variational inference with standard supervised and semi-supervised learning and naturally leads to answers to the following questions:

1. How can we do coverage tests with neural networks?
2. How are systematic uncertainties incorporated in the training process?
3. How can we do goodness-of-fit checks on neural-network predictions?

The first half of the paper is concerned with the unified viewpoint and derives the various loss functions from the joint KL-divergence. The second half then answers the three questions above.

2 Monte Carlo estimates and the joint KL-divergence

The laws of nature lead to inherently probabilistic measurements due to the uncertainty principle in quantum mechanics. Any observable that can be measured is therefore subject to fluctuations and follows a specific probability distribution. The probability distribution over possible measurement outcomes is called the likelihood function when viewed as a function of its parameters. It is a central object in both Frequentist and Bayesian statistical analyses to perform parameter estimation [6]. Its shape is entirely determined by the laws of nature in combination with the detector response. However, because the laws can be convoluted and the experiment can be very complex, it is usually not possible to write down an explicit analytic expression. A common practice is to estimate the likelihood function from Monte Carlo simulations where all these complex effects are considered [18]. This estimated likelihood function is then used to perform inference or calculate confidence intervals.

Neural networks allow to skip this estimation step completely, because the Monte Carlo samples themselves are not only drawn from the true likelihood function, but more generally from the true joint distribution $\mathcal{P}_t(x, z_o)$ of observations x and parameters of interest z_o . Let us call the corresponding true likelihood function $\mathcal{L}_t(z; x) = \mathcal{P}_t(x; z)$ where $\mathcal{P}_t(x; z)$ is the true probability distribution of the measured data x given the properties z_o . Here z_o stands for *observed* properties in the simulation, for example the position of a particle interaction. Connected to this likelihood function, there exists a true posterior distribution $\mathcal{P}_t(z_o; x)$ and a true prior distribution $\mathcal{P}_t(z_o)$. The true joint distribution follows the distribution which includes the detector response and selection effects inherent to the measurement - it also includes artificial selection effects. For example, if the generating function of the direction of injected particles is uniform, the actually recorded Monte Carlo events will generally not be uniform due to detector effects. The implicitly contained true prior $\mathcal{P}_t(z_o)$ is this non-uniform distribution over z_o of the actually registered events, not the uniform generating distribution.

Since a Monte Carlo simulation draws samples $x_i, z_{o,i}$ from the joint distribution $\mathcal{P}_t(x, z_o)$, we can always evaluate any expectation value under the true joint probability distribution as

$$E_{x, z_o}[f(x, z_o)] = \int_{x, z_o} \mathcal{P}_t(x, z_o) f(x, z_o) dx dz_o \approx \frac{1}{N} \sum_{x_i, z_{o,i}} f(x_i, z_{o,i}) \quad (1)$$

where i indexes the N samples. The following sections make use of a specific choice for f , namely $f = \ln \frac{\mathcal{P}_t(x, z_o)}{q(x, z_o)}$, which yields an expectation value that equals the KL-divergence between two distributions $\mathcal{P}_t(x, z_o)$ and $q(x, z_o)$. The KL-divergence [19] is a natural quantity to measure the distance between two probability distributions, is always positive, and often appears in statistical analysis. In particular, if q_ϕ is a parametrized probability distribution, the KL-divergence defines a natural loss function over ϕ that achieves its minimum when q_ϕ is equal to \mathcal{P}_t . It is therefore often used in *variational* methods which perform inference via optimization [20]. It turns out that the joint KL-divergence can be used to derive the loss functions in both supervised learning and unsupervised VAEs, and thereby unifies them as two connected approaches to variational inference in slightly different circumstances.

2.1 Supervised learning

The KL-divergence of the true joint distribution $\mathcal{P}_t(z_o, x)$ and an approximation $q(z_o, x)$ can be written as

$$D_{\text{KL, joint}(x, z_o)}(\mathcal{P}_t; q) = \int_x \int_{z_o} \mathcal{P}_t(z_o, x) \cdot \ln \frac{\mathcal{P}_t(z_o, x)}{q(z_o, x)} dz_o dx = \int_x \int_{z_o} \mathcal{P}_t(z_o; x) \cdot \mathcal{P}_t(x) \cdot \ln \frac{\mathcal{P}_t(z_o; x) \cdot \mathcal{P}_t(x)}{q(z_o; x) \cdot q(x)} dz_o dx \quad (2)$$

$$= \int_x \int_{z_o} \mathcal{P}_t(z_o; x) \cdot \mathcal{P}_t(x) \cdot \left(\ln \frac{\mathcal{P}_t(z_o; x)}{q(z_o; x)} + \ln \frac{\mathcal{P}_t(x)}{q(x)} \right) dz_o dx \quad (3)$$

$$= \int_x \int_{z_o} \mathcal{P}_t(x) \cdot \mathcal{P}_t(z_o; x) \cdot \ln \frac{\mathcal{P}_t(z_o; x)}{q(z_o; x)} dz_o dx + \int_x \mathcal{P}_t(x) \cdot \ln \frac{\mathcal{P}_t(x)}{q(x)} dx \quad (4)$$

$$= E_x[D_{\text{KL, Post}(z_o; x)}(\mathcal{P}_t; q)] + D_{\text{KL, Marg}(x)}(\mathcal{P}_t; q) \quad (5)$$

The distributions involving \mathcal{P}_t can not be evaluated analytically, but as discussed above Monte Carlo simulations yield samples from \mathcal{P}_t and hence provide sample based estimates of the integrals. Taking the sample estimate and parametrizing the posterior approximation $q(z_o; x)$ using a neural network with a

parameter vector ϕ , $q(z_o; x) = q_\phi(z_o; x)$, yields the following update rule over ϕ to minimize the KL-divergence objective and thereby minimize the supervised loss function $\mathcal{L}_{\text{supervised}}(\phi)$:

$$\arg \min_{\phi} \hat{D}_{\text{KL}, \text{joint}(x, z_o)}(\mathcal{P}_t; q_\phi) = \arg \min_{\phi} \frac{1}{N} \sum_{S \in x_i, z_{o,i}} \ln \left(\frac{\mathcal{P}_t(z_{o,i}; x_i)}{q_\phi(z_{o,i}; x_i)} \right) + \ln \left(\frac{\mathcal{P}_t(x_i)}{q(x_i)} \right) \quad (6)$$

$$= \arg \min_{\phi} \frac{1}{N} \sum_{S \in x_i, z_{o,i}} -\ln(q_\phi(z_{o,i}; x_i)) + \text{const} \quad (7)$$

$$= \arg \min_{\phi} \frac{1}{N} \sum_{S \in x_i, z_{o,i}} -\ln(q_\phi(z_{o,i}; x_i)) \quad (8)$$

$$\equiv \arg \min_{\phi} \mathcal{L}_{\text{supervised}}(\phi) \quad (9)$$

The approximation of the marginal likelihood, $q(x_i)$, is typically not of interest, so it can be dropped as a constant part with respect to changes in ϕ . Additionally we can drop the true posterior evaluations $\mathcal{P}_t(z_{o,i}; x_i)$ which are also constant with respect to ϕ . Instead of approximating the full joint distribution, only the posterior part is therefore explicitly approximated. The derivation shows that minimizing the KL-divergence between the true posterior and an approximation given by a neural network is equivalent to standard neural network training where the goal is to minimize negative log-probability over labels. This has been discussed previously [16], but it is usually described as a maximum likelihood objective with respect to the network parameters. Here, we emphasize that it is really more useful to think of $q_\phi(z_{o,i}; x_i)$ as a parameterized posterior over labels $z_{o,i}$ given the data x_i , not as a likelihood function with respect to the parameters ϕ . In unsupervised learning the z_i are not available so the precise above objective does not work. In the following we show that a simple replacement of the posterior KL-divergence in eq. 5 with the respective reverse KL-divergence leads to a tractable solution via the reparametrization trick [21] which contains the evidence lower bound (ELBO) and thereby the VAE objective.

2.2 Unsupervised learning: Variational autoencoders

A useful way to think of latent variables in unsupervised variational autoencoders is to imagine them as unobserved labels that are not recorded in the simulation. The implied direct comparison, and renaming, of "observed" into "unobserved" labels is justified if the latent variables have positive mutual information with the data. In particle physics, for example, if such a latent variable with positive mutual information exists, it must be a property of the particle interaction, and therefore in principle it can be labeled. Typical labels with such properties are the position or direction of a particle at the interaction point.¹ Starting with the same joint KL-divergence, but now using unobserved labels z_u , we can write

$$D_{\text{KL}, \text{joint}(x, z_u)}(\mathcal{P}_t; q) = E_x [D_{\text{KL}, \text{Post}(z_u; x)}(\mathcal{P}_t; q)] + \underbrace{D_{\text{KL}, \text{Marg}(x)}(\mathcal{P}_t; q)}_{\equiv D_{\text{KL}, \text{M}}} = E_x \left[\int_{z_u} \mathcal{P}_t(z_u; x) \cdot \ln \frac{\mathcal{P}_t(z_u; x) \cdot \mathcal{P}_t(x)}{q(z_u; x) \cdot q(x)} dz_u \right] \quad (10)$$

$$\approx \text{Surrogate}_{\text{KL}} = E_x [D_{\text{rev.KL}, \text{Post}(z_u; x)}(q; \mathcal{P}_t)] + D_{\text{KL}, \text{M}} = E_x \left[\int_{z_u} q(z_u; x) \cdot \ln \frac{q(z_u; x) \cdot \mathcal{P}_t(x)}{\mathcal{P}_t(z_u; x) \cdot q(x)} dz_u \right] \quad (11)$$

$$= E_x \left[\int_{z_u} q(z_u; x) \cdot \ln \frac{q(z_u; x)}{\mathcal{P}_t(z_u; x)} dz_u \right] + D_{\text{KL}, \text{M}} \quad (12)$$

$$= E_x \left[\int_{z_u} q(z_u; x) \cdot \ln \frac{q(z_u; x) \cdot \mathcal{P}_t(x)}{\mathcal{P}_t(x, z_u)} dz_u \right] + D_{\text{KL}, \text{M}} \quad (13)$$

$$= E_x \left[\int_{z_u} q(z_u; x) \cdot \ln \frac{q(z_u; x) \cdot \mathcal{P}_t(x)}{p(x; z_u) \cdot p(z_u)} dz_u \right] + E_x \left[\int_{z_u} q(z_u; x) \cdot \ln \frac{p(x; z_u) \cdot p(z_u)}{\mathcal{P}_t(x, z_u)} dz_u \right] + D_{\text{KL}, \text{M}} \quad (14)$$

$\underbrace{\hspace{15em}}_{D_{\text{KL}}(\mathcal{P}_t(x) \cdot q(z_u; x), p(x, z_u))} \quad \underbrace{\hspace{15em}}_{\equiv \mathcal{R}}$

¹If the number of latent variables is very large, some of them will be superfluous and not carry any information about the data. For such variables this identification strictly makes no sense since they could never be labeled.

$$= E_x[\ln \mathcal{P}_t(x)] - E_x \underbrace{\left[\int_{z_u} q(z_u; x) \cdot \left[\ln p(x; z_u) - \ln \frac{q(z_u; x)}{p(z_u)} \right] dz_u \right]}_{\text{evidence lower bound}} + \mathcal{R} + D_{\text{KL}, M} \quad (15)$$

By switching the KL-divergence with the reverse KL-divergence in eq. 11 we make the objective partially tractable while keeping the desired behavior. If $q(z_u, x) = P_t(z_u, x)$, the surrogate term becomes zero, just as the regular joint KL-divergence. This step is necessary because we have no access to samples from $\mathcal{P}_t(z_u; x)$ ². With the introduction of an auxiliary distribution $p(x, z_u)$, the surrogate KL-divergence then splits into two terms. The first term is the KL-divergence between $P_t(x) \cdot q(z_u; x)$ and $p(x, z_u)$, which is equal to the ELBO loss when the constant term $E_x[\ln \mathcal{P}_t(x)]$ is pulled out of the integral. This joint KL-divergence between $P_t(x) \cdot q(z_u; x)$ and $p(x, z_u)$ has been used before in the context of the InfoVAE [22] or more generally in the information auto-encoding family [23] and is another non-standard starting point to derive the ELBO loss. Here it arises as a necessary term in the derivation from the joint KL-divergence with the true distribution. The other term that appears is a residual term \mathcal{R} , which itself is not tractable, because any samples drawn from $q(z_u; x)$ can not be evaluated by the inaccessible density $P_t(z_u; x)$. However, it is a useful quantity that can be used in principle to gauge how far the approximation is from the truth. In fact, after a hypothetical optimization of the ELBO loss, when using flexible normalizing-flow parametrizations of q_ϕ and p_θ , we have $q(z_u; x) \cdot P_t(x) \approx p(x; z_u) \cdot p(z_u)$, and \mathcal{R} is approximately equal to the KL-divergence between $P_t(x, z_u)$ and $p(x, z_u)$ or $P_t(x, z_u)$ and $P_t(x) \cdot q(z_u; x)$. Since the KL-divergence is invariant under invertible transformations and the VAE solution is typically not unique, it really only makes sense to use this quantity in the context of identifiability theory [24]. In our view this derivation clarifies something that is typically glossed over in the literature. In most papers, going back to the original VAE paper [21], it is usually said that the approximation q_ϕ approximates the distribution p_θ which is of the same parametric family as the true model. In fact, the true model distribution is also often called p_θ , which might lead to confusion. The derivation here explicitly shows that p_θ does not represent the true model, and also does not have to be in the same family of distributions as the true model. Rather, p_θ and q_ϕ approximate each other in a consistent manner, and the resulting difference to the truth P_t can be measured by a residual term \mathcal{R} that remains positive or zero after standard ELBO optimization. The difference should then be measured up to identifiability class as defined in [24]. The introduction of the distribution $p(x, z) = p(x; z_u) \cdot p(z_u)$ in eq. 14 in this particular factorization is necessary. Without it, the term in eq. 13, excluding the true distributions \mathcal{P}_t which are intractable, would be a simple entropy term which diverges. Furthermore, its introduction has two implications. First, it creates a tractable part of the joint KL-divergence, the ELBO. Second, it offers a way to quantify the end result of the optimization of the ELBO using the residual term \mathcal{R} to measure differences from the truth \mathcal{P}_t .

In contrast to the supervised case, the joint KL-divergence is intractable and cannot be used as a loss function. We have to switch to a surrogate term using the reverse KL-divergence of the posterior, which essentially contains the same information. Further, we have to neglect the residual term \mathcal{R} by implicitly ignoring any dependence on the parameters which we denote by \mathcal{K} .

$$\arg \min_{\theta, \phi} \widehat{\text{Surrogate}}_{KL}(q_\phi, p_\theta, \mathcal{K}) \quad (16)$$

$$= \arg \min_{\theta, \phi} \widehat{D}_{KL}(\mathcal{P}_t(x) \cdot q_\phi(z_u; x), p_\theta(x, z_u)) + \text{const} \quad (17)$$

$$= \arg \min_{\theta, \phi} -\widehat{\text{ELBO}}(\theta, \phi) \quad (18)$$

$$= \arg \min_{\theta, \phi} \frac{1}{N} \sum_{S \in \mathcal{X}_i, z_{u,i,\phi}} -\ln p_\theta(x_i; z_{u,i,\phi}) + \ln \left(\frac{q_\phi(z_{u,i,\phi}; x_i)}{p(z_{u,i,\phi})} \right) \quad (19)$$

This is the standard sample-based ELBO objective of the VAE which is typically derived from the marginal likelihood.

The derivation here manifests the fact that the VAE solution of p_θ and q_ϕ does in general not agree with the truth P_t . Extra constraints on the mutual information between data and labels [22], the total correlation of latent variables [25], a better prior parametrization [26] or constraints on the data generation process [24] can be used to not only improve the ELBO but also improve the agreement with the true distribution \mathcal{P}_t and thereby decrease \mathcal{R} within a given identifiability class. A comparison of \mathcal{R} for different VAE implementations using Monte Carlo truth experiments with existing labels to calculate \mathcal{P}_t could therefore be useful for benchmarking.

²In section 2.1 we have access to the related term $\mathcal{P}_t(z; x)$ via the simulation samples which we do not have for unobserved latent variables.

2.3 Extended supervised or semi-supervised learning

Now let us assume that we have observed and unobserved latent variables z_o and z_u , respectively. The KL-divergence of the joint distribution can then be expanded into three parts as

$$D_{\text{KL},\text{joint}(x,z_o,z_u)}(\mathcal{P}_t; p_a) \quad (20)$$

$$= \int \int \int \mathcal{P}_t(z_u, z_o, x) \cdot \ln \frac{\mathcal{P}_t(z_u, z_o, x)}{q(z_u, z_o, x)} dz_u dz_o dx \quad (21)$$

$$= E_{x,z_o,z_u} \left[\ln \frac{\mathcal{P}_t(z_u; z_o, x)}{q(z_u; z_o, x)} \right] + E_{x,z_o} \left[\mathcal{P}_t(z_o; x) \cdot \mathcal{P}_t(x) \cdot \ln \frac{\mathcal{P}_t(z_o; x)}{q(z_o; x)} \right] + E_x \left[\ln \frac{\mathcal{P}_t(x)}{q(x)} \right] \quad (22)$$

$$= \underbrace{E_{x,z_o} [D_{\text{KL},\text{Post}(z_u; z_o, x)}(\mathcal{P}_t; q)]}_{\text{VAE-like term}} + \underbrace{E_x [D_{\text{KL},\text{Post}(z_o; x)}(\mathcal{P}_t; q)] + D_{\text{KL},\text{Marg}(x)}(\mathcal{P}_t; q)}_{\equiv \mathcal{S}} \quad (23)$$

$$\approx \text{Surrogate}_{\text{KL}} + \mathcal{S} \quad (24)$$

$$= E_x \left[q(z_u; z_o, x) \cdot q(z_o; x) \cdot \ln \frac{q(z_u; z_o, x)}{\mathcal{P}_t(z_u; z_o, x)} \right] + \mathcal{S} \quad (25)$$

$$= E_x \left[q(z_u; z_o, x) \cdot q(z_o; x) \cdot \ln \frac{q(z_u; z_o, x) \cdot \mathcal{P}_t(z_o, x)}{\mathcal{P}_t(z_u, z_o, x)} \right] + \mathcal{S} \quad (26)$$

$$= E_x \left[q(z_u; z_o, x) \cdot q(z_o; x) \ln \frac{q(z_u; z_o, x) \cdot \mathcal{P}_t(z_o, x)}{p(x; z_o, z_u) \cdot p(z_o, z_u)} \right] + \underbrace{E_{x,z_o} \left[q(z_u, z_o; x) \ln \frac{p(x; z_o, z_u) \cdot p(z_o, z_u)}{\mathcal{P}_t(x, z_o, z_u)} \right]}_{\equiv \mathcal{R}} + \mathcal{S} \quad (27)$$

$$= E_x [q(z_o; x) \cdot \ln(\mathcal{P}_t(z_o, x))] + E_x \left[q(z_u; z_o, x) \cdot q(z_o; x) \ln \frac{q(z_u; z_o, x)}{p(x; z_o, z_u) \cdot p(z_o, z_u)} \right] + \mathcal{R} + \mathcal{S} \quad (28)$$

where in eq. 23 the overall KL-divergence splits into an intractable term similar to the VAE derivation and a term \mathcal{S} that is similar to the supervised derivation. The intractable first term has to be replaced by a surrogate term, similar to the VAE derivation in eq. 11, that allows to draw tractable samples but contains the same information. This time, however, the surrogate loss is not unique, but we have two choices. Besides the choice for the first term made in eq. 25, we could have chosen $E_x \left[q(z_u; z_o, x) \cdot \mathcal{P}_t(z_o; x) \ln \frac{q(z_u; z_o, x)}{\mathcal{P}_t(z_u; z_o, x)} \right]$, which uses the samples from the true observed distribution for z_o instead of samples from the current approximation $q(z_o; x)$. However, for complete consistency in the sampling of z_o within goodness-of-fit procedures at all times it is more reasonable to use $q(z_o; x)$. At the end of training both choices agree since then $q(z_o; x) \cdot \mathcal{P}_t(x) \approx \mathcal{P}_t(z_o, x)$. We use this result to define two loss functions in the following.

Extended supervised loss The first is a loss definition that can be used to perform what we call *extended supervised training*, and will be important for the calculation of a goodness-of-fit as described in section 7. It is a straightforward sample based application of eq. 28, where we make use of parametrizations $q_\varphi(z_u; z_o, x)$, $p_\Psi(z_o, z_u)$ and $p_\theta(x; z_o, z_u)$:

$$\arg \min_{\theta, \phi, \varphi, \Psi} \widehat{\text{Surrogate}}_{\text{KL}}(q_\phi, p_\theta, \not{q}_\phi, \mathcal{R}) \quad (29)$$

$$= \arg \min_{\theta, \phi, \varphi, \Psi} \frac{1}{N} \sum_{S \in x_i, \underline{z}_{\theta, \tau, \phi}, z_{u, i, \varphi}} \ln(\mathcal{P}_t(z_{o, i, \phi}, x_i)) + \ln \frac{q_\varphi(z_{u, i, \varphi}; \underline{z}_{\theta, \tau, \phi}, x_i)}{p_\theta(x_i; \underline{z}_{\theta, \tau, \phi}, z_{u, i, \varphi}) \cdot p_\Psi(\underline{z}_{\theta, \tau, \phi}, z_{u, i, \varphi})} + \hat{\mathcal{S}} \quad (30)$$

$$= \arg \min_{\theta, \phi, \varphi, \Psi} \frac{1}{N} \sum_{S \in x_i, \underline{z}_{\theta, \tau, \phi}, z_{u, i, \varphi}} \ln \frac{q_\varphi(z_{u, i, \varphi}; \underline{z}_{\theta, \tau, \phi}, x_i)}{p_\theta(x_i; \underline{z}_{\theta, \tau, \phi}, z_{u, i, \varphi}) \cdot p_\Psi(\underline{z}_{\theta, \tau, \phi}, z_{u, i, \varphi})} + \underbrace{\frac{1}{N} \sum_{S \in x_i, z_{o, i}} -\ln(q_\phi(z_{o, i}; x_i))}_{\mathcal{L}_{\text{supervised}}} \quad (31)$$

$$\equiv \arg \min_{\theta, \phi, \varphi, \Psi} \mathcal{L}_{\text{ext. supervised}}(\theta, \phi, \varphi, \Psi) \quad (32)$$

The true observed labels are denoted by $z_{o, i}$ and samples from q_ϕ are denoted by $\underline{z}_{\theta, \tau, \phi}$ where the dash again denotes the gradient is not propagated. The motivation to make the gradient of $\ln(\mathcal{P}_t(\underline{z}_{\theta, \tau, \phi}, x_i))$ with respect to ϕ vanish and drop it along \mathcal{R} comes from the fact that it is intractable in this particular choice of surrogate loss. If previously the other choice for the surrogate loss had been made, the samples $\underline{z}_{\theta, \tau, \phi}$ would be replaced by the true labels $z_{o, i}$ and the term would be constant, i.e. have a vanishing gradient, automatically. Not propagating the gradient with respect to ϕ via $\underline{z}_{\theta, \tau, \phi}$ also separates the first sum in eq. 31 from the second sum with respect to the parameters ϕ . Instead of training the extended supervised loss in one training run, one can also choose to first train the supervised part, i.e. the second sum, and only later train the rest. An extended supervised training can therefore always be started with an already finished supervised model and can be viewed as an add-on to it.

Semi-supervised learning The extended supervised loss can also be adapted for semi-supervised learning. In semi-supervised learning parts of the training data have labels, and parts are unlabeled. In the derivation of the VAE loss we argued that latent variables that share mutual information with the data can in principle be labeled. In semi-supervised learning, this assumption is automatically implied - parts of the data are not labeled, but could be in principle. Taking the variational viewpoint of the previous sections, a naive solution might be to use the supervised loss for data with labels, the VAE-loss for data without labels, and use the same distribution q_ϕ in both losses to share parameters. A more natural solution, however, seems to be the following:

$$\arg \min_{\theta, \phi, \varphi, \Psi} \mathcal{L}_{\text{semi-supervised}}(\theta, \phi, \varphi, \Psi) \quad (33)$$

$$= \arg \min_{\theta, \phi, \varphi, \Psi} \begin{cases} \mathcal{L}_{\text{ext.supervised}}(\theta, \phi, \varphi, \Psi) & \text{(labeled data)} \\ \frac{1}{N} \sum_{S \in \mathcal{X}_i, \mathcal{Z}_{o,i,\phi}, \mathcal{Z}_{u,i,\varphi}} \ln \frac{q_\varphi(\mathcal{Z}_{u,i,\varphi}; \mathcal{Z}_{o,i,\phi}, \mathbf{x}_i) \cdot q_\phi(\mathcal{Z}_{o,i,\phi}; \mathbf{x}_i)}{p_\theta(\mathbf{x}_i; \mathcal{Z}_{o,i,\phi}, \mathcal{Z}_{u,i,\varphi}) \cdot p_\Psi(\mathcal{Z}_{o,i,\phi}, \mathcal{Z}_{u,i,\varphi})} & \text{(unlabeled data)} \end{cases} \quad (34)$$

To remain with the previous notation, the z_u denote extra unobserved latent variables and collect all the extra information in the event. For labeled data, the extended supervised loss is used, and the $z_{o,i}$ denote true label information. For unlabeled data, the $z_{o,i}$ are unobserved and are sampled from q_ϕ to effectively create an ELBO-like loss with latent variable $z = \{z_o, z_u\}$. The only difference is a sign flip and different sampling strategy, which ultimately can be traced back to the difference between the standard and reverse KL-divergence. Because the parametrization does not change for data with or without labels, only the sampling strategy differs, this Ansatz seems to be an elegant and natural way to unify both types of data.

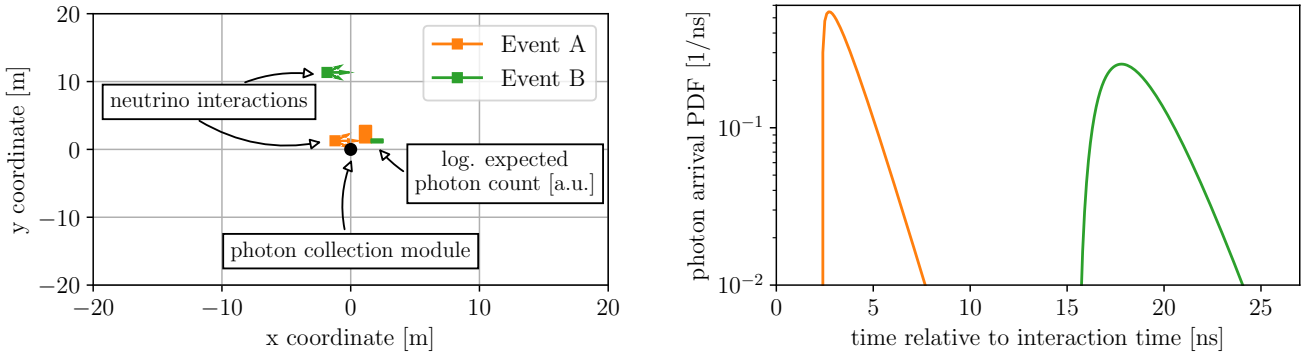
3 Toy Monte Carlo

A toy Monte Carlo dataset has been created to perform empirical tests in the following sections. It is designed to mimic electromagnetic showers of electron-neutrino interactions [27] in a Cherenkov neutrino detector like IceCube [8] in a 2-D setting. In reality, such showers consist of charged particles that emit Cherenkov light in a coherent light front at the Cherenkov angle that changes its shape as detection modules are further away from the interaction point [28]. For ice, which is the detection medium in IceCube, the light front becomes nearly isotropic for large distances. In general, depending on the position and orientation of the shower with respect to a detection module, the shape of the resulting arrival time distribution of photons varies. In this toy simulation the arrival time distribution is parametrized by a gamma distribution. In addition, the expected number of detected photons falls off exponentially with distance and depends on the orientation of the shower with respect to the module. The actual number of observed photons follows a Poisson distribution. Fig. 1 illustrates the various datasets that are used in the next sections.

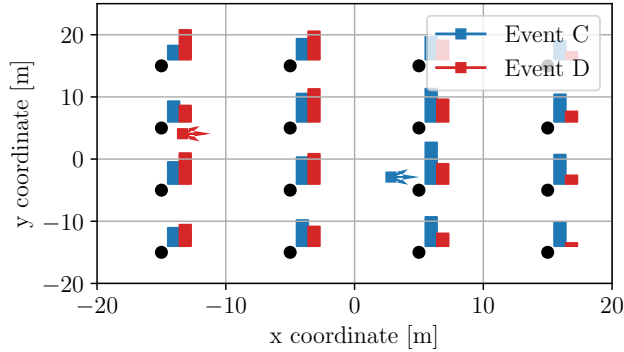
Fig. 1 (a) shows a detector that consists of a single module with two example neutrinos A and B . The two bars next to the photon collection module indicate the logarithmic expected mean of the number of observed photons from each neutrino interaction. Fig. 1 (b) shows the two corresponding photon arrival distributions. For event A , the data distribution is more concentrated than for event B , because the particle interacts closer to the detection unit. Also the number of observed photons is larger. Fig. 1 (c) shows the configuration of a second set of Monte Carlo simulations for a larger detector and a simulated threshold condition that at least 5 photons are observed for an event to be recorded. Also depicted are two associated example events (C and D) together with their expected number of photons in the various photon collection modules. Dataset 1 and 2 have two intrinsic degrees of freedom, the position of each neutrino interaction. The deposited energy and thereby emitted photons is always the same. A third dataset has an additional degree of freedom by also randomizing the direction. A fourth and fifth dataset are variants of dataset 2 with a constrained event generation region and track-like instead of point-like energy depositions, respectively. A summary of all datasets is given in table 1. The detection process can be described by an inhomogeneous tempo-spatial Poisson point process [29]. The spatial part is restricted to the position of the collection modules, while the temporal detection can happen at all times. The corresponding likelihood function for observed labels z_o is an extended likelihood [30], which can be written as

$$\mathcal{L}(z_o; \mathbf{k}, \mathbf{t}) = \mathcal{P}_t(\mathbf{k}, \mathbf{t}; z_o) = \prod_{j=1}^N \frac{\exp^{-\lambda_j(z_o)} \cdot \lambda_j(z_o)^{k_j}}{k_j!} \prod_{i=1}^{k_j} p_j(t_i; z_o) \quad (35)$$

where for a total number of modules N , λ_j is the expectation value of a Poisson distribution for module j , k_j the detected number of photons in module j , and $p_j(t_i)$ the photon arrival probability distribution in module j with observed photon times t_i .



(a) Dataset 1 (a single photon collector) with two example events A and B. All events point towards the positive x-axis. (b) Photon arrival time distributions of events A and B.



(c) Dataset 2 (16 photon collectors) with two example events C and D. All events point towards the positive x-axis.

Figure 1: Illustration of neutrino toy Monte Carlo datasets. The photon collection modules detect a Poisson distributed number of photons whose arrival time follows a certain distribution. The mean for the Poisson distribution and arrival time per photon depends on the orientation and position of the neutrino interaction relative to a given photon collection module.

	no. modules	d.o.f.	event	other
dataset 1	1	2 (pos.)	point-like	> 1 detected photon
dataset 2	16	2 (pos.)	point-like	> 5 detected photons
dataset 3	16	3 (pos.+dir.)	point-like	> 5 detected photons
dataset 4	16	2 (pos.)	point-like	> 5 detected photons, $ x < 10\text{m}$, $ y < 10\text{m}$
dataset 5	16	2 (pos.)	track-like	> 5 detected photons

Table 1: Properties of the datasets used for various comparisons. The detector geometry is always similar to dataset 1 or dataset 2 as depicted in fig. 1.

4 The importance of flow-based models

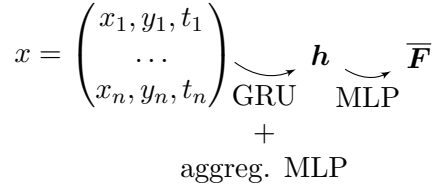
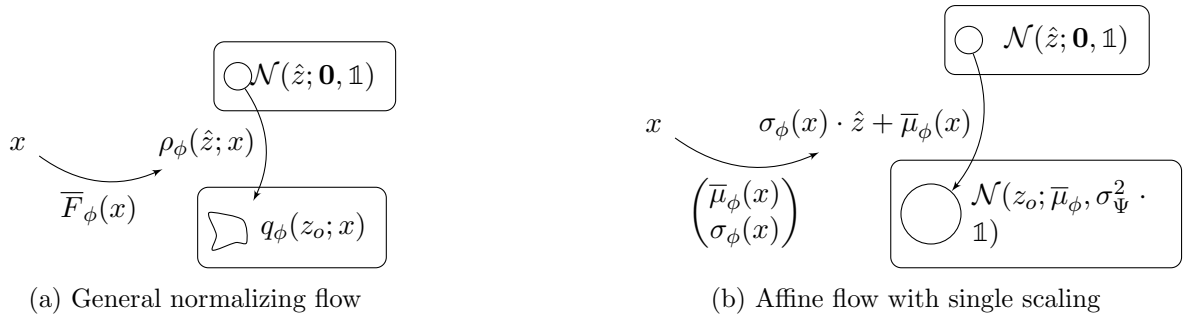
All derivations so far assumed non-specific parametrizations of conditional probability density functions, i.e. posteriors and likelihoods, with neural networks. A general way to parametrize a probability density function with a neural network is via normalizing flows [17]. An invertible transformation $z_o = \rho_\phi(\hat{z})$ transforms a base random variable \hat{z} , in this case following a standard normal distribution, to the desired target random variable z_o . This transformation is typically parametrized by a neural network with parameters ϕ . Denoting the probability density of the base by $p_b(\hat{z})$ and the target by $q(z_o)$ we can calculate the log-probability of the target

$$\ln(q(z_o)) = \ln(p_b(\rho^{-1}(z_o))) - \ln(\det(J_{\hat{z}}^{\rho_\phi})) \quad (36)$$

where $J_{\hat{z}}^{\rho_\phi}$ is the Jacobian of ρ_ϕ with respect to \hat{z} . Flows can be composed of multiple other flows $\rho = \rho_1 \circ \rho_2 \cdots \circ \rho_n$ and the resulting log-probability simply involves a sum over all log-determinants. In general $p_b(\hat{z})$ can be arbitrary, but for simplicity and the possibility to calculate coverage (see section 6) we use the standard normal distribution. One can also generate samples from $q(z_o)$ by first sampling \hat{z}_i from $p_b(\hat{z})$ and then transform the samples via $z_{o,i,\phi} = \rho_\phi(\hat{z}_i)$, where the samples now depend on the network parameters ϕ . This makes the samples differentiable, known as the reparametrization trick [21], and is a key feature in the variational autoencoder and extended supervised losses (section 2.3). A natural way to make the resulting probability distribution conditional on x , i.e. describe $q(z_o; x)$, is to make the transformation ρ dependent on x , as indicated in fig. 2 (a). In general, a neural network that takes x as an input predicts the parameters \bar{F} , which in turn defines $\rho_\phi(\hat{z}; x) = \rho(\hat{z}; \bar{F}_\phi(x))$. As a specific example, fig. 2 (b) shows an affine flow where a neural network predicts a mean vector $\bar{\mu}$ and a width σ when the base distribution is a standard normal distribution. The resulting probability distribution $q_\phi(z_o; x)$ of this flow describes a symmetric Gaussian distribution with mean $\bar{\mu}$ and standard deviation σ . This is a common choice in some regression problems in high-energy neutrino physics [31] and used later in some comparisons. The most common choice in supervised learning is to fix $\sigma = 1$, which results in a Gaussian PDF with unit variance which corresponds to the Mean-Squared-Error (MSE) loss function. Generic flows with a standard normal distribution as base distribution therefore naturally generalize the MSE-loss.

In all further comparisons, we split the parameters of flow-based posteriors into two parts. The first part consists of an encoder with gated recurrent units (GRUs) [32] and a subsequent aggregate MLP to encode the data into an internal representation \mathbf{h} . The GRU reads in a time-ordered sequence of photons, where each photon is characterized by its detected position and time. The second part is a multi-layer perceptron with 2 layers that further maps that internal representation to the respective flow parameters \bar{F} . The process is illustrated in fig. 2 (c). At the end of training we adopt stochastic weight averaging (SWA) [33]. We found this to reduce the fluctuations and find a rather stable "mean posterior solution". More details on the architecture and also on the training procedure is given in appendix A.

With the likelihood function (eq. 35) and the inherent prior distribution we can construct a true posterior distribution. In the following we assume a flat prior for simplicity. We can then compare the true posterior with the posterior approximations obtained using various normalizing flows after training. Fig. 3 shows such a comparison for the example events from the previous section. It compares a flexible Gaussianization flow [34] with an affine flow (see fig. 2 for details). For dataset 1, which consists of a single photon collection module, the resulting posterior is highly non-Gaussian. The flexible Gaussianization flow can approximate the posterior much better than an affine flow with a single width parameter. For dataset 2 the events generally contain more observed photons and the posteriors become more Gaussian-like. Both flows have more comparable shapes in this example. To assess performance more generally, fig. 4 shows the posterior approximation quality versus the number of parameters of the second part of the flow. The number of parameters of the first GRU encoder part is held fixed and not included in the quantity displayed on the x-axis. The second part, which consists of an MLP with two layers, is varied in its hidden dimension. For the Gaussianization flow, additionally the number of flow parameters is varied, which specifically for Gaussianization flows leads to more internal layers and more kernel basis elements (see appendix A for details). In general, the flexible Gaussianization flow is more parameter efficient than the simpler affine flow. The MSE loss yields a posterior that only by chance is roughly the same scale than some posteriors for dataset 2, while for dataset 1 it is completely off and therefore not shown. The better parameter efficiency of the Gaussianization flow has to do with the possibility to adjust the potential complexity of the flow itself, i.e. increase the size of \bar{F} . For an affine flow, on the other hand, \bar{F} is fixed to be a mean $\bar{\mu}$ and width σ , and one can only increase the complexity by increasing the MLP hidden dimension. In all cases, the final performance saturates, where more parameters do not help performance. We interpret this as a bottleneck of the GRU encoder, since the Gaussianization flow should in principle be flexible enough to describe all true posterior shapes in the training dataset. We come back to this point in the discussion at the very end of the paper.



(c) Common data encoding for all experiments.

Figure 2: General flow (a) and a specific affine flow (b) parametrization of the approximate posterior in supervised learning. Choosing $\sigma_\phi = 1$ yields a shifted standard normal distribution which is the PDF used in the MSE loss. The common encoding scheme for all experiments is depicted in (c).

5 Systematic Uncertainties

A standard practice to incorporate systematics in a both Frequentist and Bayesian analyses is to first assume they can be parametrized by a parameter ν which follows a statistical distribution, typically a Gaussian with a known mean and width, e.g. $p(\nu; \mu_\nu, \sigma_\nu)$. Such a parametrization does not make sense in a Frequentist sense, but should rather be understood subjectively as the ignorance about the true value of the systematic parameter ν in question. In a Frequentist analysis every systematic is then included as a quadratic penalty term in the likelihood function, corresponding to the Gaussian assumption, with respective nuisance parameters in a profile likelihood approach [35]. In a Bayesian analysis the systematic uncertainties influence the joint distribution of x and θ , i.e. $p(x, \theta) \rightarrow p(x, \theta; \nu)$. A marginalized joint density can then be obtained as $\mathcal{P}_{t,M}(x, \theta) = \int p(x, \theta; \nu) p(\nu) d\nu$. Because it applies to the joint distribution, it also applies to any term in Bayes' theorem,

$$\mathcal{P}_t(\theta; x, \nu) = \frac{\mathcal{P}_t(x; \theta, \nu) \mathcal{P}_t(\theta; \nu)}{\mathcal{P}_t(x; \nu)} \quad (37)$$

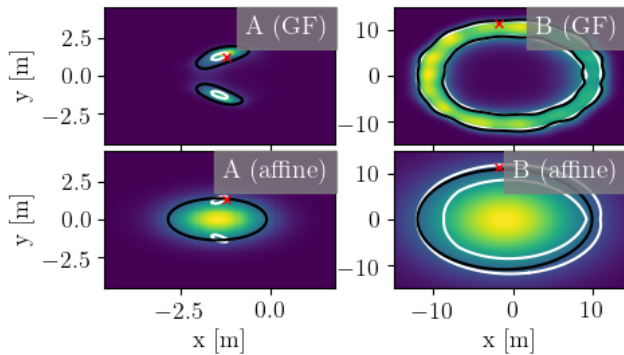
and one can for example obtain the marginalized posterior as

$$\mathcal{P}_{t,M}(\theta; x) = \int \mathcal{P}_t(\theta; x, \nu) \cdot p(\nu) d\nu \quad (38)$$

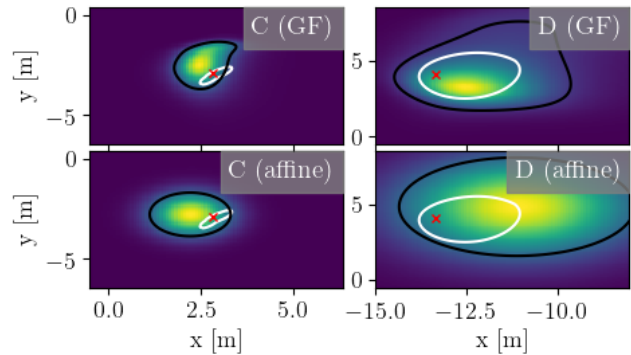
which now includes the extra uncertainty about the systematics parameter ν . A Monte Carlo simulation that first draws systematic parameters ν and then records events with labels θ and data x according to the detector response will automatically produce samples from $\mathcal{P}_{t,M}(\theta, x)$ or any true conditional distribution of interest. Incorporating systematic uncertainties into all loss functions defined in the previous sections is therefore straight forward, because all of them rely on samples drawn from the joint distribution. For supervised learning, for example, one can just replace any term P_t by $P_{t,M}$ in eq. 5 and the neural network based approximation q_ϕ will approximate the marginalized true posterior $\mathcal{P}_{t,M}(\theta; x)$. It is common practice in modern high-energy physics experiments to generate Monte Carlo simulations with potentially marginalized systematic parameters [36], so there is no overhead in actually including those uncertainties. The next section illustrates the coverage behavior of the variational posterior including such marginalization.

6 Coverage of the neural network posterior

In Frequentist or Bayesian analyses it is important to know how well confidence or credible intervals cover the true values. In a Frequentist analysis, in the limit of large amounts of data, Wilks' Theorem [37] implies that the quantity $\lambda = -2 \cdot (\ln L(\theta_t) - \ln L(\theta_0))$ is χ_ν^2 distributed with ν corresponding to the dimensionality of θ when θ_0 is the value that maximizes the likelihood function and θ_t the true value that generated the data. It is connected to the fact that likelihood scans around the optimum have an approximately Gaussian shape

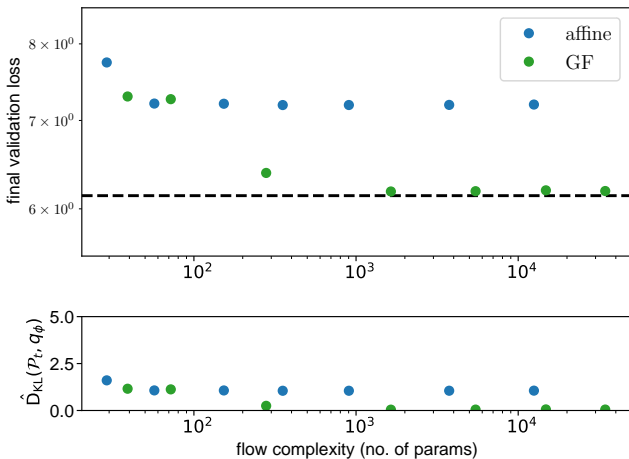


(a) Posterior scans of dataset 1 example events.

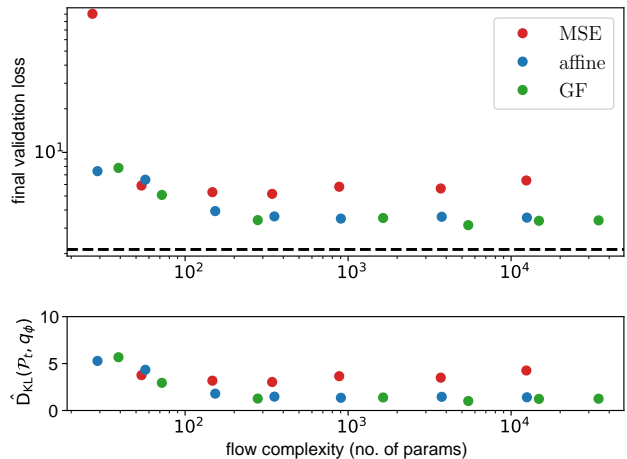


(b) Posterior scans of dataset 2 example events.

Figure 3: A comparison of posteriors of the position for the example events A and B from dataset 1 and events C and D from dataset 2. The normalizing flow posterior is shown together with a 68% contained probability mass in black. The 68% probability mass contour of the true posterior assuming a flat prior is shown in white. The true event positions are marked in red. The upper row shows the result for Gaussianization flows, the lower row for an affine flow (a Gaussian) with a single covariance parameter.



(a) Performance vs. complexity for dataset 1.



(b) Performance vs. complexity for dataset 2.

Figure 4: Posterior approximation performance of a Gaussianization flow [34] (GF), an affine flow with a single variable width σ (affine), and an affine flow with $\sigma = 1$ (MSE). Along the x-axis the number of parameters and the potential flow complexity increases, while the encoding complexity is held fixed (see text). The respective upper plot shows the validation loss. The black dotted line shows the loss obtained from the true posterior. The respective lower plot shows the sample-based KL divergence.

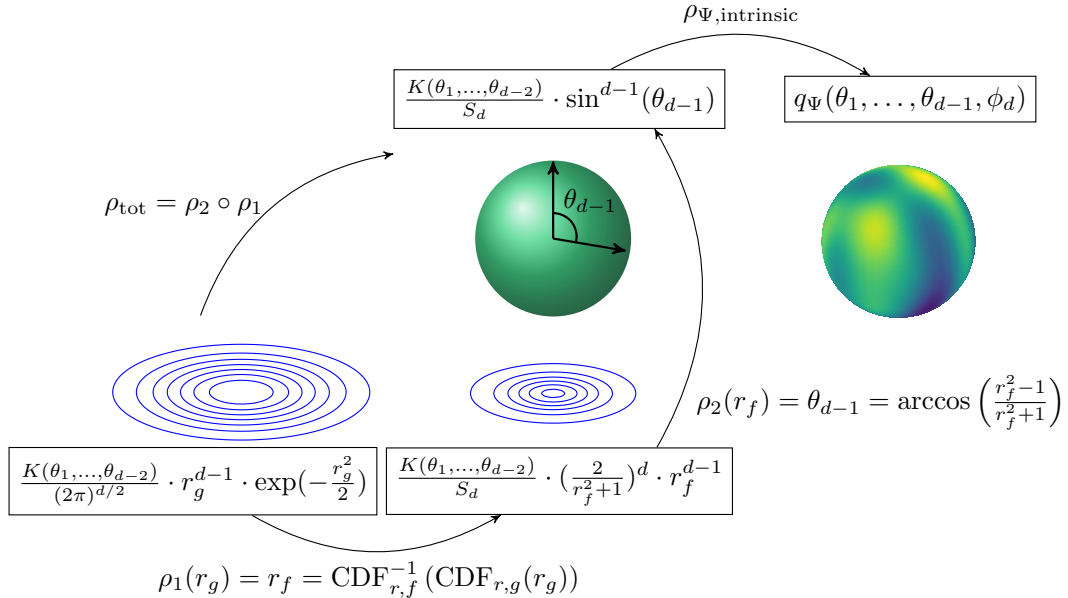


Figure 5: Illustration of a stable normalizing flow q_Ψ on the d -sphere starting with a d -dimensional standard normal distribution to allow for exact coverage calculation. The flows ρ_1 and ρ_2 involve only the radial coordinate due to rotational symmetry. The second flow ρ_2 is equal to the stereographic projection with a hyper plane that splits the sphere into two hemispheres. This is different from the visualization for illustrative purposes.

in the large-data limit. A similar statement appears in a Bayesian analysis from the Bernstein-von-Mises theorem [38], which implies that for large amounts of data the posterior $p(\theta; x)$ becomes Gaussian. For any n -dimensional multivariate Gaussian the quantity $(x - \mu)C^{-1}(x - \mu)$ is χ_n^2 distributed [39], which again implies the quantity $\lambda_{\text{Bayes}} = -2 \cdot (\ln p(\theta_t; x) - \ln p(\theta_0; x))$ is also χ^2 distributed in the Gaussian limit of $p(\theta; x)$.

Both of these coverage calculations require the assumption of the large-data limit. With normalizing flows that have a Gaussian distribution as base distribution, we can use the same methodology to calculate exact coverage for a target distribution of *any* shape. By construction, samples following a target $q_\phi(z_o)$ are generated by drawing samples \hat{z}_i from a base normal distribution $p_b(\hat{z})$, for simplicity we use a standard normal, and apply $\rho(\hat{z})$. We can invert this logic and for any target sample $z_{o,i}$ that we would like to test flow back to the Gaussian base using $\hat{z}_i = \rho^{-1}(z_{o,i})$. If the samples $z_{o,i}$ follow the target $q_\phi(z_o)$, the corresponding samples \hat{z}_i at the base must follow a standard normal distribution, and this implies the quantity $\lambda_{\text{base}} = -2 \cdot (\ln p_b(\hat{z}) - \ln p_b(0))$ is again χ^2 distributed. The whole process is illustrated in fig. 6 (f).

We can further extend this coverage calculation to posteriors on manifolds like spheres. In [40] the authors discuss how to define a flexible normalizing flow on a sphere via stereographic projection of a normalizing flow in the plane. A more stable alternative turns out to be directly to start with a base distribution on the sphere and parametrize a flexible flow which is intrinsic to the manifold [41]. We can combine both of these ideas to define a flexible flow on the sphere that also allows to define coverage. The methodology is illustrated in fig. 5 and consists of multiple sub-flows.

The base distribution is again a standard normal distribution in \mathbb{R}^n . It is transformed to another distribution in \mathbb{R}^n that itself corresponds to the flat distribution on the n -sphere once it is stereographically projected. Then follows the stereographic projection, and finally the intrinsic flow on the sphere. The first two flows from the standard normal in \mathbb{R}^n to the flat distribution on the sphere can be combined without actually invoking a Riemannian manifold flow which normally would involve the calculation of the gram matrix $J^T J$ where J would be the jacobian of the given manifold mapping. To do so, the distributions in the plane are first written in spherical coordinates. The radial coordinate of the Gaussian distribution in \mathbb{R}^n is then transformed to θ_{d-1} on the sphere, while the remaining angular coordinates $(\theta_1, \dots, \theta_{d-2}, \phi)$ stay unchanged. The end result of these transformations turns out to be (see appendix B for a derivation)

$$\rho_{\text{tot},1} = \left(\theta_1, \dots, \theta_{d-2}, \phi, \pi \cdot (1 - \text{erf}(r_g/\sqrt{2})) \right) \quad (d = 1) \quad (39)$$

$$\rho_{\text{tot},2} = \left(\theta_1, \dots, \theta_{d-2}, \phi, \arccos(1 - 2 \cdot \exp(-r_g^2/2)) \right) \quad (d = 2) \quad (40)$$

for the special cases of the 1-sphere and 2-sphere, respectively. For higher-dimensional spheres, no analytical function for the radial part can be written down, but individual sub-parts of the flow are analytical. Evaluations and inverses can be obtained using bisection and a potentially Newton iterations if derivatives are desired.

To demonstrate coverage, fig. 6 (a)+(b) illustrate expected versus actual coverage for learning a 2-d (position) and 3-d (position and 1-d direction) posterior in the supervised learning setting. The 2-d calculation employs a 2-dimensional Gaussianization flow [34] trained dataset 2. The 3-d posterior is trained on dataset 3, in which as an additional degree of freedom also the direction of neutrino interactions is randomized. We use a factorized posterior $q_\phi(x_p, y_p, \theta; x) = q_{\phi_1}(x_p, y_p; x) \cdot q_{\phi_2}(\theta; x_p, y_p, x)$, which allows to learn the spherical part separately from the euclidean part in a stable manner. While the euclidean part again uses a 2-d Gaussianization flow, the spherical part employs the previously described strategy to reach a flat distribution on the 1-sphere (eq. 39) and afterwards uses convex Moebius transformations [41] parametrized by a neural network as an intrinsic flow. Coverage is calculated by flowing both flows backwards to a joint 3-d standard normal distribution. This is an example for coverage of a joint posterior defined on $\mathbb{R}^2 \times \mathcal{S}^1$, but the methodology works analogously for general dimensions.

We can observe interesting coverage behavior during training. In both example cases, initially the posteriors either under- or over-cover. Once the first phase of training is over, in which the loss function decreases rapidly, good coverage is already reached, even though the overall training has not finished yet. The learning curves of the two training runs are depicted in fig. 6 (c)+(d). The second phase, in which the optimization is much slower has been called "random diffusion phase" by [42]. The authors argue the network learns a better compression of the input data in this stage. In the context of normalizing flows, it seems the first phase brings the learned posteriors in line with the labels to reach proper coverage. In the second diffusion phase, the posterior regions shrink as much as they can while maintaining coverage.

To illustrate the effect of systematic uncertainties on the resulting coverage, fig. 6 (e) shows the coverage curve for a "systematic" dataset where the expected photon count in each module is marginalized with a Gaussian with a relative width of 50%. Including the systematic marginalization leads to slight over-coverage with respect to the true labels which is the desired behavior.

7 Goodness-of-Fit of the neural network model

The coverage calculation is only a meaningful information for data that is similar to the training data. If new input data is given to a fully trained neural network, for example real data instead of a Monte Carlo simulation, it is desirable to test if this new data can be described by the neural network model. If this is the case then the coverage results might apply³. Traditionally, a test between a model and data is done via a goodness-of-fit test. In the following we describe how the extended supervised training procedure described in section 2.3 allows to calculate a goodness-of-fit via posterior predictive simulations. The structure of the extended supervised model is shown in fig. 7. On top of a posterior q_ϕ , we have an additional posterior over unobserved latents q_ψ , and a prior p_ψ and likelihood p_θ as a generative model. Posterior predictive simulations are a standard methodology in Bayesian analysis to do goodness-of-fit tests of the resulting posterior distribution [43]. A p-value can be defined via

$$p = \int_{x,z} \mathbf{I}_{T(x,z) > T(x_{\text{obs}}, z)} p_\theta(x; z) q_\phi(z; x_{\text{obs}}) dx dz \quad (41)$$

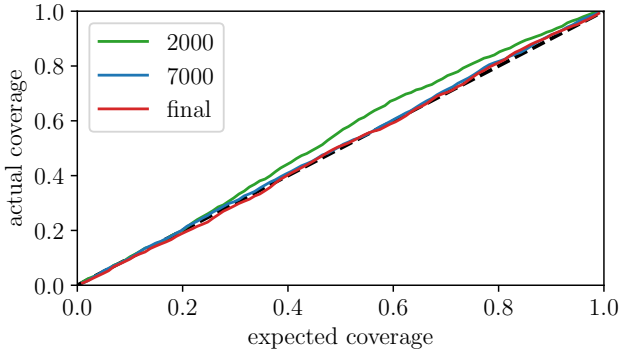
which can be numerically calculated using samples from $p_\theta(x; z) \cdot q_\phi(z; x_{\text{obs}})$ which is the posterior predictive distribution. The quantities $T(x, z)$ are called test quantities, and $\mathbf{I}_{T(x,z) > T(x_{\text{obs}}, z)}$ the indicator function, where the integral effectively counts the fraction of samples where $T(x_i, z_i) > T(x_{\text{obs}}, z_i)$ for an infinite number of samples x_i, z_i . A comparison of a given p-value with the ensemble of p-values from the training dataset gives a goodness-of-fit criterion. In contrast to Frequentist goodness-of-fit testing, the test quantities also depend on the parameter z , and the expected p-value distribution is not uniform, but usually more peaked around 0.5. Only in certain limits, for example for infinitely precise posterior distributions, does the p-value distribution approach the uniform distribution [43]. This means, one has to determine the p-value distribution for the training dataset, and then calculate the p-value for any new data event and compare it to the training distribution. We propose to use the logarithm of the likelihood divided by the number of data points N_d ,

$$T(x, z) = \ln p_\theta(x; z) / N_d \quad (42)$$

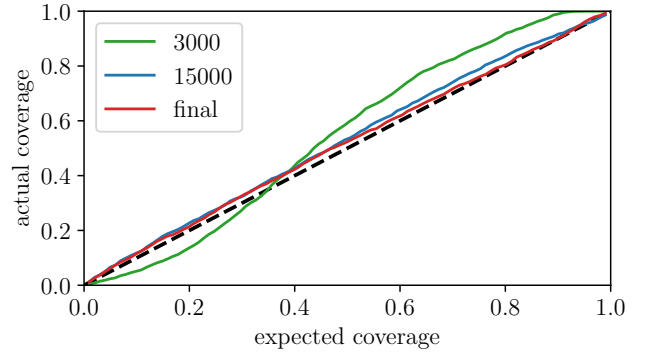
$$(43)$$

as a test quantity. The division by N_d is required for the Poisson process likelihood, in which different data realizations have a different number of observed counts, and the division makes them effectively comparable. For other likelihoods, or a test quantity based on the posterior distribution, this division would not be necessary. We omit a test quantity based on the posterior, because data realizations of events at the border of the detector sometimes have zero counts, and no meaningful posterior can be calculated in this case because we do not train on such events. However, this might be a viable alternative in situations where this does not happen. Any test quantity based on the likelihood or posterior can readily be calculated since they

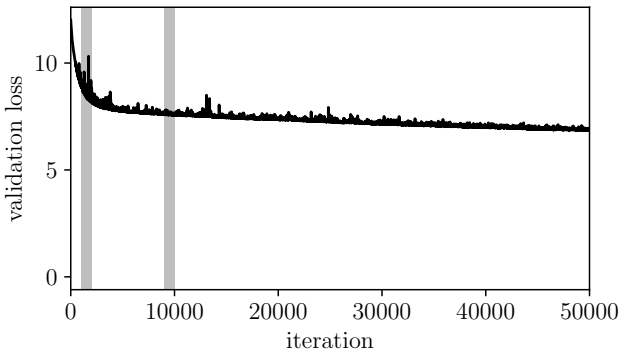
³We presume coverage is calculated using the validation dataset and that validation and training dataset are sufficiently similar.



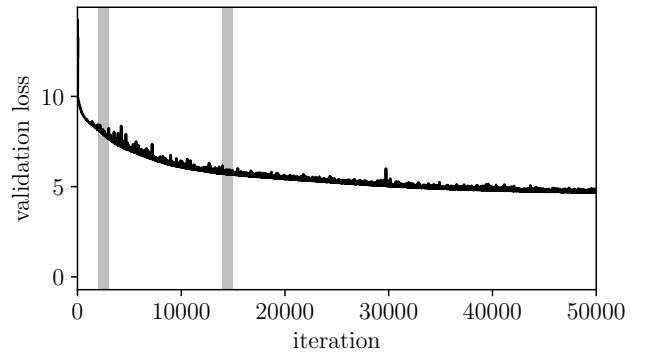
(a) Coverage of 3-d posteriors using dataset 3 for different stages of training.



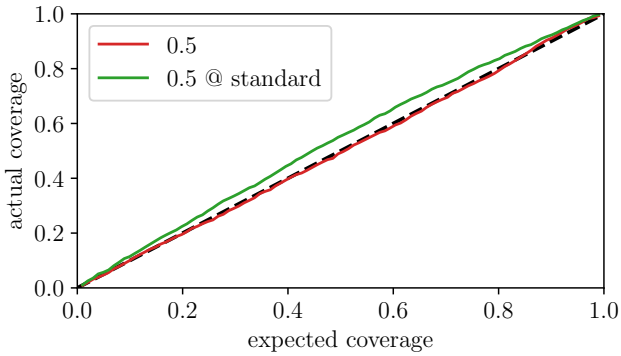
(b) Coverage of 2-d posteriors using dataset 2 for different stages of learning.



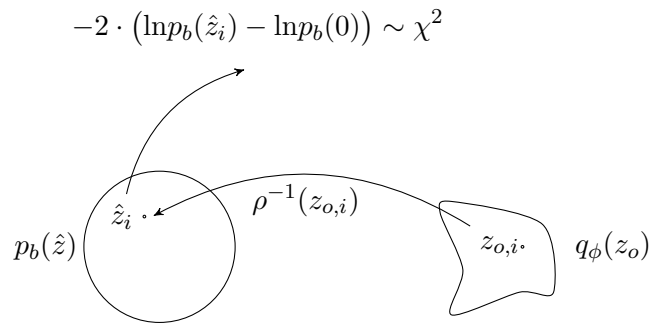
(c) Validation loss curve for 3-d posteriors.



(d) Validation loss curve for 2-d posteriors.



(e) Coverage for a dataset trained on marginalized photon light yield expectation (red) and applied to a standard dataset (green).



(f) Illustration of χ^2 behavior in the base distribution.

Figure 6: Illustration of coverage for a 2-d (a) and 3-d (b) posterior calculated for the validation dataset. The respective learning curves are shown for 2-d (c) and 3-d (d), including intervals where the models are averaged using SWA for earlier coverage calculation in comparison to coverage obtained at the end of training (final). A coverage calculation for a marginalized systematic dataset is shown in (e) applied to itself (red) and a dataset with the true value of the systematic parameter (green). The coverage principle is indicated in (f).

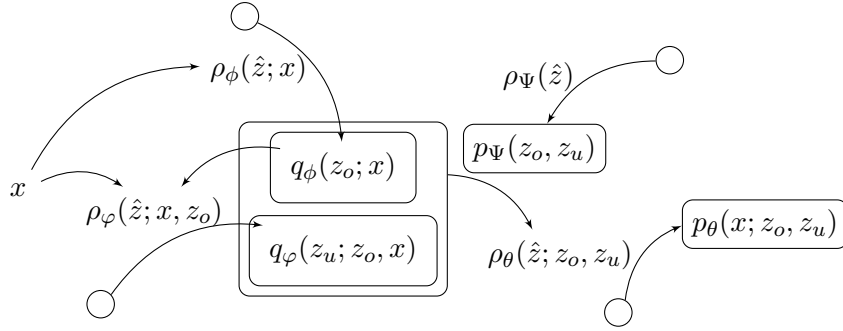


Figure 7: Generic structure of the extended supervised loss for goodness-of-fit tests and semi-supervised applications based on four normalizing flows. The respective auxiliary unit-gaussian random variables \hat{z} are denoted by circles and the respective flow-defining functions by ρ .

are part of the extended supervised training procedure. In order to illustrate the calculation, the extended supervised training is performed on dataset 4. This dataset is similar to dataset 2, but only consists of neutrino interactions inside the detector whose absolute magnitude in either x or y coordinate is smaller than 10m. Because it intrinsically only has two degrees of freedom, the two coordinates of position of the interaction, and both of them are predicted by the posterior q_ϕ , we leave out the latent posterior q_ϕ for simplicity. In our case for Poisson process data, the likelihood p_θ has to model eq. 35, and is a hybrid of a part that models the Poisson distribution, and another part that defines the continuous PDF via a normalizing flow. Details are given in appendix A. The p-value distribution of this training dataset is shown in fig. 8. as the red curve. In addition, two other p-value distributions are depicted, where the same model

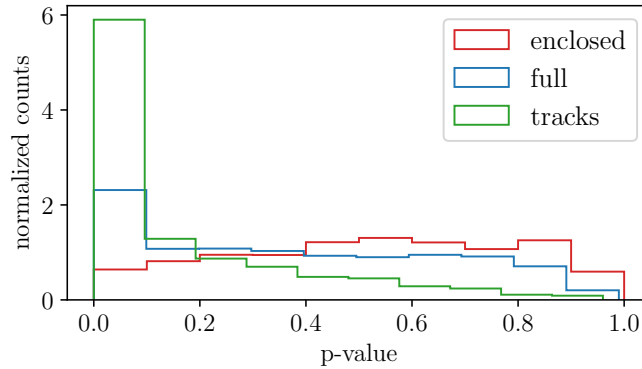


Figure 8: Goodness-of-fit p-value distribution for three datasets. The model is trained on dataset 5, which consists of contained neutrino interactions (red). The p-values are also calculated for a dataset of all neutrino interactions (dataset 2 - blue) and a dataset consisting of 20m long tracks of light emission (dataset 5 - green) to emulate muon tracks.

is applied to events from dataset 2 and dataset 5. Dataset 2 contains additional events at the boundary of the detector, but is otherwise similar. Dataset 5 emulates muon tracks as 20m track-like energy depositions with similar energy deposition than the point-like interactions. As can be seen, the p-value distribution for the training dataset is more or less symmetric around 0.5, although a slight shift to larger p-values remains, possibly because the training result is located in a local optimum or not fully converged. Dataset 2 contains a peak for very low p-values, which is dominated by events at the boundary of the detector. An even stronger skew in the distribution is seen for muon tracks, whose signature is even more different on average than the training sample. This example is obtained with toy simulations that only qualitatively model a situation commonly encountered in neutrino telescopes. However, it illustrates that it is in principle possible to train an extended supervised model on a signal dataset, apply the resulting model to any data event, and based on the resulting p-value decide to keep the event or exclude it from further analysis. The remaining events should be similar to events from the training sample, within uncertainties given by the training statistics and any included systematics. Besides such an application for data selection, it might also be interesting to study goodness-of-fit results for concrete data to Monte carlo comparisons or for data anomaly detection.

8 Related Work

We discussed that standard supervised training can be viewed as variational inference, and variational inference can be viewed as an approximate likelihood-free inference approach. An active topic in likelihood-free inference are neural sequential inference procedures [44]. These procedures typically require guided re-simulations for a single event, and eventually should converge to the true posterior. From our perspective, simple supervised learning with normalizing flows, in combination with coverage and goodness-of-fit guarantees as described earlier, seems more suited for applications in high-energy physics where time is often critical and posteriors for large datasets might be desired. Even for single astronomical multi-messenger alerts [10], given the discussed coverage and goodness-of-fit checks, an initial posterior that can be trusted can be sent to the community quickly. One can later always decide to refine the result with an iterative likelihood-free procedure like automatic posterior transformation (APT) [45] which would naturally blend in due to its use of normalizing flows. For gravitational waves, posterior inference with autoregressive flows has been discussed recently in [15]. In this line of work, coverage is checked with 1-dimensional marginal distributions which seems more computationally demanding than our approach. Systematics or goodness-of-fit tests are not discussed in that paper. In another related line of research, normalizing flows have been used to model the likelihood function directly [13]. Pure likelihood modeling inherits some problems of the standard likelihood machinery: a time consuming optimization or MCMC procedure. However, in our view it is useful to model the likelihood as the generative part in the proposed "extended supervised training" (section 2.3), but always in combination with an associated posterior. A central part of our derivation is based on the joint KL-divergence. The importance of the joint KL-divergence has been emphasized in other approximate Bayesian inference, for example to unify expectation propagation in Gaussian processes [46] and as mentioned earlier for the derivation of the supervised loss for neural networks [16]. In the latter example, however, the loss function is not called the log-posterior, but conditional maximum likelihood objective with respect to the neural network parameters. While both views are correct, the posterior interpretation is more fruitful in our opinion, in particular in combination with normalizing flows which shows that supervised learning can behave as rather well-approximated variational inference. Another related recent work applied normalizing flows for a neutrino oscillation analysis [47]. The authors do not use the joint KL-divergence in the derivation, which makes it less obvious how to include systematics, although they briefly mention one approach among two alternatives that is similar to our suggestion. The authors also argue for a vague agreement of the base distribution with a Gaussian after training, but do not discuss quantifiable coverage tests.

9 Conclusion

In the first part of the paper we have shown that the supervised learning loss, a semi-supervised learning loss, an extended supervised loss and the unsupervised ELBO-loss of variational autoencoders can all be derived under one unifying theme of variational inference. The inference in all these approaches can be traced back to the minimization of the KL-divergence between the true joint distribution of data and labels and an approximation for certain sub-parts of the joint distribution based on neural networks.

For supervised learning, the derivation of the loss function from the KL-divergence of the joint distribution is well-known but the connection to variational inference of the posterior distribution is typically not being made. From our perspective, however, this interpretation is very useful in high-energy physics, even when using an MSE loss function which has very poor approximating power. After all, a central task of a physics analysis is to calculate a posterior distribution, and the variational perspective shows that neural networks learn to predict exactly that. Normalizing flows with a standard normal base naturally generalize the MSE loss, and are crucial to make the variational inference perspective usable in practice.

A simple replacement of observed with unobserved labels in the KL-divergence allows to eventually derive the ELBO loss of variational autoencoders. In this derivation, the usual encoder q_ϕ and decoder p_θ are both manifestly auxiliary, and are explicitly separated from the true distribution \mathcal{P}_t which p_θ and q_ϕ both try to approximate within a given identifiability class of transformations. This is different from the usual derivation via the marginal likelihood, e.g. as discussed in the original VAE paper [21], where p_θ is often used to denote both the true posterior and the recognition model, which obfuscates the fact that those are typically not the same and also do not have to be the same parametric class.

Normalizing flows with a Gaussian as a base distribution, which for simplicity we choose as a standard normal, have a second advantage. They can be used to calculate coverage for the n -dimensional probability density function $q_\phi(z_o; x)$ they describe. Flowing a test input back to the base distribution, $\hat{z}_i = \rho^{-1}(z_{o,i})$, allows to calculate the quantity $\lambda_{\text{base}} = -2 \cdot (\ln p_b(\hat{z}_i) - \ln p_b(0))$ which should be χ_n^2 distributed if the input follows $q_\phi(z_o; x)$. A similar procedure is known from classical Frequentist coverage calculations. The important difference is that the normalizing-flow coverage calculation works for arbitrary posterior distributions $q_\phi(z_o; x)$. We further expanded the idea to calculate coverage for arbitrary distributions on spheres \mathcal{S}^m , or more generally to joint posteriors on $\mathbb{R}^n \times \mathcal{S}^m$. To enable coverage for such distributions we derived the transformation from the n -dimensional standard normal Gaussian to the flat distribution on the n -sphere, which for 1 and 2 dimensions is conveniently simple and invertible. A further intrinsic flow on the sphere can

then describe a more complex distribution. This two-step procedure ensures stable training, since starting with the flat distribution on the sphere is a more stable training process than deforming a distribution in the plane and afterwards stereographically project it, as was already pointed out in [41].

We demonstrated such a coverage calculation with a 2-d posterior of position x, y and with a joint 3-d posterior of position and direction x, y, θ for point-like neutrino interactions in a toy Monte Carlo. Empirically, we observed that coverage is already obtained once the training phase enters the random diffusion phase as defined by [42]. Since the loss still decreases during this phase, only more slowly, and in the variational interpretation this implies shrinking posteriors, in this second training phase the posterior approximations get slowly better while coverage stays intact.

Viewing all these models as coming from the joint KL-divergence makes it also natural to include systematic uncertainties in the final approximated posterior distributions. They are included via Bayesian marginalization of the true posterior which can be included during the Monte Carlo generation process. We test the result with a coverage calculation for a dataset where the number of expected observed photons is marginalized with a Gaussian to emulate a systematic uncertainty. The resulting posterior regions are larger which leads to the desired over-coverage with respect to the original dataset.

Finally, we test the *extended supervised learning* scheme. It is related to semi-supervised learning and involves a hybrid of the supervised and VAE losses. In addition to the posterior q_ϕ , a latent encoder q_φ , a prior p_ψ , and a decoder p_θ are learned either jointly or separately as an add-on to the supervised posterior q_ϕ . The extra latent encoder q_φ learns further latent variables to encode information not captured by the posterior, while the prior and decoder define a generative model. The combination of a posterior and a generative model allows to perform Bayesian predictive simulations, which in combination with a test quantity $T(x, z)$, which we suggest to be the (reduced) log-likelihood function⁴, allows to calculate a p-value which can be used as a goodness-of-fit criterion. Any data, that is not similar to the training data within the given uncertainty of the statistical approximations of the neural networks, leads to p-values close to 0 and can be excluded. We test this concept with a neural network model trained on point-like neutrino interactions contained in the center of the detector. In comparison with point-like interactions in the full detector, the model calculates a small p-value for events on the boundary of the detector. We also apply it on a dataset containing track-like energy depositions mimicking muon tracks, for which the separation is also markedly visible. Such a goodness-of-fit selection strategy can potentially allow a very simple data selection. Any data which is sufficiently different from the training data can be removed by a simple selection based on the p-value.

Let us mention two aspects that require further investigation. The first is related to the stability of the training algorithm and the final learned distributions. We used stochastic weight averaging to average over several iterations at the end of training to obtain a more stable posterior solution. This serves as an approximation to ensemble averaging, which is basically averaging under a variational posterior over network weights. Due to varying learning rates for different model complexities, slight fluctuations in the final loss values remained (see fig. 4). Ideally, one would like a scheme where repeated training schedules lead to repeatable posterior regions which are indistinguishable within a certain margin which can be defined before training. This needs to be studied more systematically.

A second aspect is related to the data encoding. In all studies we have split the conditional posterior into a data encoding based on a GRU and aggregate MLP, and a second MLP which further maps that encoding to the normalizing flow parameters. Our Monte Carlo tests show that at some level of flow complexity the performance bottleneck of the posterior approximation comes from the data-encoding part. It will therefore be interesting to study more powerful encoding strategies, and potentially identify an optimal encoding for Poisson process data, which is the dominant data type in high-energy physics. Any improvement in data encoding will not only translate to tighter posterior contours, but also to a more powerful goodness-of-fit calculation.

Acknowledgements

We thank Alexander Trettin for suggesting a more realistic parametrization for the toy Monte Carlo.

A Implementation details

A.1 Training

All training procedures use a sample-based natural gradient descent (NGD) [48] with a diagonal approximation and running averages of the mean and diagonal fisher matrix. We observed this to converge much faster for normalizing flows than ADAM [49] or standard stochastic gradient descent (SGD) [50]. One can also interpret this as a natural gradient version of ADAM. We use a mostly fixed learning rate which adjusts itself to keep fluctuations of the validation loss at a certain level. For the affine flows, we had to fix the

⁴The log-likelihood divided by the number of observed data points, which is required for meaningful comparisons of observations in Poisson processes.

learning rate completely, because too large learning rates would sometimes lead to drastic jumps in the loss function. This seems to be a problem that only occurs for flows which are defined by less than a handful of parameters. For Gaussianization flows [34], similar behavior could be seen for single-layer flows with a single basis function. Once the number of flow parameters is increased beyond a certain level, it does not seem to be an issue anymore. Towards the end of training, once the loss reaches a more or less constant level, the final iterations are averaged using stochastic weight averaging (SWA) [33]. As argued by the authors, SWA approximates model ensemble averages. Model averages, in turn can be interpreted as expectations under the approximate weight posterior since SGD iterations itself can be interpreted as samples from a variational approximation of the weight posterior [51].

A.2 Posterior

The posterior parametrization is indicated in fig. 2 (c). The first encoding part is similar for all experiments. A GRU encodes the input data sequentially, the output is aggregated and mapped by a single layer MLP to a hidden dimension that summarizes the data. The aggregation is motivated for the case when more than one GRU layer is used. We choose a single-layer GRU with hidden dimension 10 and for the aggregation MLP choose intermediate dimension 15 and map to a 20-dimensional hidden dimension for all experiments in the paper. This first part has roughly 1000 parameters.

The second step in the posterior is another MLP that maps the hidden dimension to the respective flow parameters. We use two inner layers for this second MLP, and vary its number of dimensions for the various experiments. The parameter choices are described in section A.4.

A.3 Likelihood

In our case for Poisson process data, the likelihood p_θ has to model eq. 35, and is a hybrid of a part that models the Poisson distribution, and another part that defines the continuous PDF via a normalizing flow. The parameter choices are described below.

A.4 Parameter choices

In fig. 4 the number of dimension in the two inner layers of the second MLP varies between 1 and 100. For the Gaussianization flow, additionally the number of flow layers varies between 1 and 5, and the number of basis elements per flow varies between 1 and 10. For the systematic coverage test (section 6) and the goodness of fit test (section 7), the dimension of the second MLP inner layers is 50, and we use 5 Gaussianization flow layers with 5 basis elements each. For the goodness-of-fit prior, we use similar number of flow parameters and optimize over them directly, instead of feeding in a data representation. For the goodness-of-fit likelihood, we use a normalizing flow again with similar number of parameters for the continuous part of the Poisson process likelihood (eq. 35). The input are the labels and the module position in (x,y) coordinates. For the poisson part we map the labels and (x,y) dom position via a 2-layer MLP with 100 hidden units each to the logarithmic mean expectation of a Poisson distribution.

B Coverage for spheres

The following calculation derives the transformation ρ_{tot} from the d-dimensional Gaussian distribution to the flat distribution on the d-sphere (see fig. 5) which is discussed in section 6. The flow can be split up as $\rho_{\text{tot}} = \rho_2 \circ \rho_1$. The first flow ρ_1 transforms the standard normal to a distribution p_f that corresponds to the distribution in the plane that is the stereographic projection of the flat distribution on the sphere. We can derive p_f by starting with the flat distribution on the sphere. The flat distribution on the d-sphere is defined as [52]

$$p_{\text{flat,sphere}} = \frac{\sin(\theta_1)^1 \cdot \dots \cdot \sin(\theta_{d-1})^{d-1}}{S_d} = \frac{K(\theta_1, \dots, \theta_{d-2}) \cdot \sin(\theta_{d-1})^{d-1}}{S_d} \quad (44)$$

where the sine factors start to appear at dimension two. The factor K abbreviates the first $d - 2$ of those factors and S_d denotes the surface area of the d-sphere. Note that θ_1 to θ_{d-1} take values between 0 and π , and an additional angle ϕ takes values values between 0 and 2π . We then define a flow $\rho_2^{-1} = (\theta_1, \dots, \theta_{d-2}, \phi, \rho_2^{-1}(\theta_{d-1}))$ which is similar to a stereographic projection to the plane and which just transforms the last spherical coordinate θ_{d-1} , while all other angles are left unchanged. The angle θ_{d-1} is always related to the d th embedding space coordinate x_d via $x_d = \cos(\theta_{d-1})$ ⁵. In 3-dimensional space, for example, x_d equals the z coordinate. At the same time, for a stereographic projection onto a plane which aligns to split the sphere and has plane coordinates \mathbf{x}_p , it is known [53] that the relation of the embedding

⁵Note that for $d = 1$ the angle ϕ , which normally is defined with respect to (1,0) and goes from 0 to 2π , has to be redefined as $\theta_0 = \phi + \frac{\pi}{2}$ in order for this relation to hold. The angle θ_0 further goes from 0 to π , similar to the other θ_{d-1} , and is measured with respect to the "north pole" of the sphere.

coordinate x_d to the plane coordinates is given by $x_d = \frac{(\sum x_{p,j})^2 - 1}{(\sum x_{p,j})^2 + 1} = \frac{r_f^2 - 1}{r_f^2 + 1}$, which is expressed here entirely as a connection to the radial coordinate in the plane via $r_f = \sum x_{p,j}$. It therefore follows that

$$\theta_{d-1} = \arccos\left(\frac{r_f^2 - 1}{r_f^2 + 1}\right) \equiv \rho_2(r_f) \quad (45)$$

or vice versa

$$r_f = \sqrt{\frac{2}{1 - \cos(\theta_{d-1})} - 1} \equiv \rho_2^{-1}(\theta_{d-1}) \quad (46)$$

which is a relation that is indicated in fig. 5. Applying the flow ρ_2^{-1} to the flat distribution on the sphere we obtain

$$p_f(\theta_1, \dots, \theta_{d-2}, \phi, r_f) = p_{\text{flat, sphere}}(\theta_1, \dots, \theta_{d-2}, \phi, \rho_2(r_f)) \cdot \left| \frac{d\rho_2(r_f)}{dr_f} \right| \quad (47)$$

$$= \frac{K(\theta_1, \dots, \theta_{d-2})}{S_d} \cdot \left(1 - \left(\frac{r_f^2 - 1}{r_f^2 + 1}\right)^2\right)^{(d-1)/2} \cdot \frac{2}{r_f^2 + 1} \cdot r_f^{d-1} \quad (48)$$

$$= \frac{K(\theta_1, \dots, \theta_{d-2})}{S_d} \cdot \left(\frac{2}{r_f^2 + 1}\right)^d \cdot r_f^{d-1} \quad (49)$$

where p_f is now the corresponding PDF in the plane after the stereographic projection. We now need to find the flow ρ_1 (indicated in fig. 5) to transform a standard normal Gaussian distribution to p_f or vice versa. Similar to the transformation from the sphere to plane, this transformation can be done entirely focussing on the radial coordinate when the Gaussian distribution is written in spherical coordinates. The radial transformation can be calculated using the cumulative distribution functions of the radial PDFs. The two radial PDFs are

$$p_{r,g}(r_g) = \int_{\theta_1, \dots, \theta_{d-2}, \phi} \frac{K(\theta_1, \dots, \theta_{d-2})}{(2\pi)^{d/2}} \cdot r_g^{d-1} \cdot \exp\left(-\frac{r_g^2}{2}\right) d\theta_1 \dots d\theta_{d-2} d\phi \quad (50)$$

$$= \frac{S_{d-1}}{(2\pi)^{d/2}} r_g^{d-1} \cdot \exp\left(-\frac{r_g^2}{2}\right) \quad (51)$$

and

$$p_{r,f}(r_f) = \int_{\theta_1, \dots, \theta_{d-2}, \phi} \frac{K(\theta_1, \dots, \theta_{d-2})}{S_d} \cdot \left(\frac{2}{r_f^2 + 1}\right)^d \cdot r_f^{d-1} d\theta_1 \dots d\theta_{d-2} d\phi \quad (52)$$

$$= \frac{S_{d-1}}{S_d} \cdot \left(\frac{2}{r_f^2 + 1}\right)^d \cdot r_f^{d-1} \quad (53)$$

where $p_{r,g}$ is the radial distribution of the d-dimensional standard normal distribution and $p_{r,f}$ the radial distribution of p_f . The corresponding CDFs which map from \mathbb{R}^+ to $[0, 1]$ then follow to be ⁶

$$\text{CDF}_{r,g} = \frac{S_{d-1}}{2 \cdot (\pi)^{d/2}} \cdot (\Gamma(d/2) - \Gamma(d/2, r_g^2/2)) \quad (\text{general } d) \quad (54)$$

$$\text{CDF}_{r,g,1} = \text{erf}(r_g/\sqrt{2}) \quad (d = 1) \quad (55)$$

$$\text{CDF}_{r,g,2} = 1 - \exp(-r_g^2/2) \quad (d = 2) \quad (56)$$

and

$$\text{CDF}_{r,f} = \frac{S_{d-1} \cdot (2 \cdot r_f)^d}{S_d \cdot d} \cdot {}_2F_1(d/2; d; d/2 + 1; -r_f^2) \quad (\text{general } d) \quad (57)$$

$$\text{CDF}_{r,f,1} = \frac{2}{\pi} \cdot \tan^{-1}(r_f) \quad (d = 1) \quad (58)$$

$$\text{CDF}_{r,f,2} = \frac{r_f^2}{r_f^2 + 1} \quad (d = 2) \quad (59)$$

⁶Evaluated using *Wolfram Alpha* at <http://www.wolfram-alpha.com>. The calculation of $\text{CDF}_{r,g}$ likely involves variable substitution, integration by parts, and then an identification with the upper incomplete gamma function. The calculation of $\text{CDF}_{r,f}$ likely involves variable substitution and an iterative application of hypergeometric identities.

where $\Gamma(x, y)$ is the upper incomplete Gamma function and ${}_2F_1$ is the Gauss hypergeometric function. The transformation ρ_1 then can be written with the corresponding CDFs as

$$r_f = \rho_1(r_g) = \text{CDF}_{r,f}^{-1}(\text{CDF}_{r,g}(r_g)) \quad (60)$$

which can in general not be written down analytically except for $d = 1$ and $d = 2$. Using bisection and Newton iterations it is possible to evaluate this expression and its inverse for higher d . The Newton iterations make the result differentiable, which is required if it is to be used in variational autoencoders. Finally, the transformation $\rho_{\text{tot}} = \rho_2 \circ \rho_1$ can be written as

$$\theta_{d-1} = \rho_{\text{tot}}(r_g) = \rho_2 \left(\text{CDF}_{r,f}^{-1}(\text{CDF}_{r,g}(r_g)) \right) \quad (\text{general } d) \quad (61)$$

$$\rho_{\text{tot},1}(r_g) = \pi \cdot (1 - \text{erf}(r_g/\sqrt{2})) \quad (d = 1) \quad (62)$$

$$\rho_{\text{tot},2}(r_g) = \arccos(1 - 2 \cdot \exp(-r_g^2/2)) \quad (d = 2) \quad (63)$$

$$(64)$$

, which has a simple and invertible structure for $d = 1$ and $d = 2$ after some manipulation with trigonometric identities, while higher dimensions again require bisection and Newton iterations. Because ρ_{tot} defines a flow from the d -dimensional standard normal distribution to the flat distribution on the d -sphere, besides its usage in normalizing flows for coverage as describe in section 6, it can be used as a non-standard way to generate uniform samples on the d -sphere. This can be done by first sampling from the d -dimensional standard normal distribution, switching to spherical coordinates, and finally transforming the radial coordinate to the last coordinate θ_{d-1} on the sphere using ρ_{tot} , while keeping all other angles $\theta_1, \dots, \theta_{d-2}$ and ϕ as they are.

References

- [1] Alex Krizhevsky, Ilya Sutskever, and Geoffrey E Hinton. Imagenet classification with deep convolutional neural networks. In *Advances in neural information processing systems*, pages 1097–1105, 2012.
- [2] Dan Guest, Kyle Cranmer, and Daniel Whiteson. Deep learning and its application to lhc physics. *Annual Review of Nuclear and Particle Science*, 68(1):161–181, 2018.
- [3] Patrick T. Komiske, Eric M. Metodiev, and Matthew D. Schwartz. Deep learning in color: towards automated quark/gluon jet discrimination. *JHEP*, 01:110, 2017.
- [4] Thomas Murach, Michael Gajdus, and Robert Daniel Parsons. A Neural Network-Based Monoscopic Reconstruction Algorithm for H.E.S.S. II. *PoS, ICRC2015:1022*, 2016.
- [5] J. Ahrens et al. Muon track reconstruction and data selection techniques in AMANDA. *Nucl. Instrum. Meth. A*, 524:169–194, 2004.
- [6] Byron P Roe. *Probability and statistics in experimental physics*. Springer Science & Business Media, 2012.
- [7] M. G. Aartsen, M. Ackermann, J. Adams, J. A. Aguilar, M. Ahlers, M. Ahrens, C. Alispach, and K. Andeen. Cosmic ray spectrum and composition from PeV to EeV using 3 years of data from IceTop and IceCube. *prd*, 100(8):082002, October 2019.
- [8] MG Aartsen, M Ackermann, J Adams, JA Aguilar, M Ahlers, M Ahrens, D Altmann, K Andeen, T Anderson, I Ansseau, et al. The icecube neutrino observatory: instrumentation and online systems. *Journal of Instrumentation*, 12(03):P03012, 2017.
- [9] BP Abbott, R Abbott, R Adhikari, P Ajith, Bruce Allen, G Allen, RS Amin, SB Anderson, WG Anderson, MA Arain, et al. Ligo: the laser interferometer gravitational-wave observatory. *Reports on Progress in Physics*, 72(7):076901, 2009.
- [10] A. Keivani, D. Veske, S. Countryman, I. Bartos, K. R. Corely, Z. Marka, and S. Marka. Multi-messenger Gravitational-Wave + High-Energy Neutrino Searches with LIGO, Virgo and IceCube. In *36th International Cosmic Ray Conference (ICRC2019)*, volume 36 of *International Cosmic Ray Conference*, page 930, July 2019.
- [11] Yarin Gal and Zoubin Ghahramani. Dropout as a bayesian approximation: Representing model uncertainty in deep learning. In *Proceedings of the 33rd International Conference on International Conference on Machine Learning - Volume 48, ICML16*, page 10501059. JMLR.org, 2016.
- [12] Balaji Lakshminarayanan, Alexander Pritzel, and Charles Blundell. Simple and Scalable Predictive Uncertainty Estimation using Deep Ensembles. *Advances in Neural Information Processing Systems*, page 64026413, December 2017.

- [13] Kaze WK Wong, Gabriella Contardo, and Shirley Ho. Gravitational-wave population inference with deep flow-based generative network. *Physical Review D*, 101(12):123005, 2020.
- [14] Alvin J. K. Chua and Michele Vallisneri. Learning bayesian posteriors with neural networks for gravitational-wave inference. *Phys. Rev. Lett.*, 124:041102, Jan 2020.
- [15] Stephen R Green, Christine Simpson, and Jonathan Gair. Gravitational-wave parameter estimation with autoregressive neural network flows. *arXiv preprint arXiv:2002.07656*, 2020.
- [16] James Martens. New insights and perspectives on the natural gradient method. *arXiv preprint arXiv:1412.1193*, 2014.
- [17] George Papamakarios, Eric Nalisnick, Danilo Jimenez Rezende, Shakir Mohamed, and Balaji Lakshminarayanan. Normalizing flows for probabilistic modeling and inference. *arXiv preprint arXiv:1912.02762*, 2019.
- [18] Nathan Whitehorn, Jakob van Santen, and Sven Lafebre. Penalized Splines for Smooth Representation of High-dimensional Monte Carlo Datasets. *Comput. Phys. Commun.*, 184:2214–2220, 2013.
- [19] S Kullback and RA Leibler. On information and sufficiency, *annals maths. Statist*, 22:79–86, 1951.
- [20] David M. Blei, Alp Kucukelbir, and Jon D. McAuliffe. Variational inference: A review for statisticians. *Journal of the American Statistical Association*, 112(518):859–877, 2017.
- [21] Diederik P Kingma and Max Welling. Auto-Encoding Variational Bayes. *arXiv e-prints*, page arXiv:1312.6114, December 2013.
- [22] Shengjia Zhao, Jiaming Song, and Stefano Ermon. Infovae: Information maximizing variational autoencoders. *arxiv. Learning*, 2017.
- [23] Shengjia Zhao, Jiaming Song, and Stefano Ermon. The information autoencoding family: A lagrangian perspective on latent variable generative models. *arXiv preprint arXiv:1806.06514*, 2018.
- [24] Ilyes Khemakhem, Diederik Kingma, Ricardo Monti, and Aapo Hyvarinen. Variational autoencoders and nonlinear ica: A unifying framework. In *International Conference on Artificial Intelligence and Statistics*, pages 2207–2217, 2020.
- [25] Hyunjik Kim and Andriy Mnih. Disentangling by factorising. *arXiv preprint arXiv:1802.05983*, 2018.
- [26] Jakub M Tomczak and Max Welling. Vae with a vampprior. *arXiv preprint arXiv:1705.07120*, 2017.
- [27] M. Tanabashi and et al. Review of particle physics. *Phys. Rev. D*, 98:030001, Aug 2018.
- [28] Leif Radel and Christopher Wiebusch. Calculation of the Cherenkov light yield from electromagnetic cascades in ice with Geant4. *Astropart. Phys.*, 44:102–113, 2013.
- [29] Yu. A. Kutoyants. *Statistical Inference for Spatial Poisson Processes*. 1998.
- [30] Roger Barlow. Extended maximum likelihood. *Nuclear Instruments and Methods in Physics Research Section A: Accelerators, Spectrometers, Detectors and Associated Equipment*, 297(3):496–506, 1990.
- [31] Sebastiano Aiello et al. Event reconstruction for KM3NeT/ORCA using convolutional neural networks. 4 2020.
- [32] Kyunghyun Cho, Bart Van Merriënboer, Dzmitry Bahdanau, and Yoshua Bengio. On the properties of neural machine translation: Encoder-decoder approaches. *arXiv preprint arXiv:1409.1259*, 2014.
- [33] Pavel Izmailov, Dmitrii Podoprikin, Timur Garipov, Dmitry Vetrov, and Andrew Gordon Wilson. Averaging weights leads to wider optima and better generalization, 2018.
- [34] Chenlin Meng, Yang Song, Jiaming Song, and Stefano Ermon. Gaussianization flows. *arXiv preprint arXiv:2003.01941*, 2020.
- [35] Kyle Cranmer. Practical statistics for the lhc. *CERN-2014-003*, pages 267 – 308, 2011.
- [36] MG Aartsen, M Ackermann, J Adams, JA Aguilar, M Ahlers, C Alispach, B Al Atoum, K Andeen, T Anderson, I Anseau, et al. Efficient propagation of systematic uncertainties from calibration to analysis with the snowstorm method in icecube. *Journal of Cosmology and Astroparticle Physics*, 2019(10):048, 2019.

- [37] S. S. Wilks. The large-sample distribution of the likelihood ratio for testing composite hypotheses. *Ann. Math. Statist.*, 9(1):60–62, 03 1938.
- [38] A. W. van der Vaart. *Asymptotic Statistics*. Cambridge Series in Statistical and Probabilistic Mathematics. Cambridge University Press, 1998.
- [39] Glen Cowan. *Statistical data analysis*. Oxford university press, 1998.
- [40] Mevlana C. Gemici, Danilo Rezende, and Shakir Mohamed. Normalizing Flows on Riemannian Manifolds. *arXiv e-prints*, page arXiv:1611.02304, November 2016.
- [41] Danilo Jimenez Rezende, George Papamakarios, Sébastien Racanière, Michael S Albergo, Gurtej Kanwar, Phiala E Shanahan, and Kyle Cranmer. Normalizing flows on tori and spheres. *arXiv preprint arXiv:2002.02428*, 2020.
- [42] Ravid Shwartz-Ziv and Naftali Tishby. Opening the black box of deep neural networks via information, 2017.
- [43] Andrew Gelman, John B. Carlin, Hal S. Stern, and Donald B. Rubin. *Bayesian Data Analysis*. Chapman and Hall/CRC, 2nd ed. edition, 2004.
- [44] Conor Durkan, George Papamakarios, and Iain Murray. Sequential neural methods for likelihood-free inference. *arXiv preprint arXiv:1811.08723*, 2018.
- [45] David S. Greenberg, Marcel Nonnenmacher, and Jakob H. Macke. Automatic posterior transformation for likelihood-free inference. In *ICML 2019*, 2019.
- [46] Thang D. Bui, Josiah Yan, and Richard E. Turner. A unifying framework for gaussian process pseudo-point approximations using power expectation propagation. *J. Mach. Learn. Res.*, 18(1):36493720, January 2017.
- [47] Sebastian Pina-Otey, Federico Sánchez, Vicens Gaitan, and Thorsten Lux. Likelihood-free inference of experimental neutrino oscillations using neural spline flows. *Phys. Rev. D*, 101:113001, Jun 2020.
- [48] S. Amari. Natural gradient works efficiently in learning. *Neural Computation*, 10(2):251–276, 1998.
- [49] Diederik P. Kingma and Jimmy Ba. Adam: A Method for Stochastic Optimization. *arXiv e-prints*, page arXiv:1412.6980, December 2014.
- [50] Lon Bottou. Large-scale machine learning with stochastic gradient descent. In *in COMPSTAT*, 2010.
- [51] Stephan Mandt, Matthew D. Hoffman, and David M. Blei. A variational analysis of stochastic gradient algorithms. In *Proceedings of the 33rd International Conference on International Conference on Machine Learning - Volume 48*, ICML16, page 354363. JMLR.org, 2016.
- [52] L. E. Blumenson. A derivation of n-dimensional spherical coordinates. *The American Mathematical Monthly*, 67(1):63–66, 1960.
- [53] Jnos Kollr. Algebraic hypersurfaces. *Bull. Amer. Math. Soc.*, pages 543–568, 2019.